

A Mesh-free Analysis of Shell Structures

C. T. Wu, Yong Guo

Livermore Software Technology Corporation

Hui-Ping Wang, Mark E. Botkin

General Motors

Abstract

A mesh-free formulation based on the Mindlin-Reissner shell theory for geometrical and material nonlinear analysis of shells is presented. In this mesh-free formulation, two projection methods are developed to generate the shell surface using the Lagrangian mesh-free interpolations. The updated Lagrangian theory underlying the co-rotational procedure is adopted for the local strain, stress and internal force updating. A local boundary integration method in conjunction with the selective reduced integration method is introduced to enforce the linear exactness and relieve shear locking. Both nonlinear static and dynamic analysis of shell structures with finite rotations are considered. Several numerical examples are presented to demonstrate the accuracy and applicability of the proposed formulation.

1. Introduction

Recent developments in mesh-free methods provide an additional dimension to computational mechanics [1-5]. Those methods do not rely on the conventional grid approach to define approximation functions. In comparison with the conventional finite element methods, the smoothness of the approximation, exemption from meshing, and higher convergence rate make the mesh-free methods attractive alternative numerical techniques for nonlinear analysis of industrial applications. Recently, several advances have been made to enhance the computational efficiency [6-9].

Most mesh-free methods have been developed for two- and three-dimensional solid applications. Several mesh-free shells have also been proposed in the content of geometrically nonlinear analysis of Kirchhoff shell [10] and Mindlin shell [11] using total Lagrangian formulations. The total Lagrangian formulation has found wide applications in problems involving geometrically non-linearity and elastic stability [12]. The updated Lagrangian formulation may be particularly useful for shell analysis involving both geometrical and material non-linearity. The development of mesh-free methods to general nonlinear shell problems still remains one of the challenging topics in the mesh-free method today.

The objective of this work is to develop a mesh-free shell for the general industrial applications with desired accuracy and wide applicabilities. In this work, two projection methods are developed to generate the shell mid-surface using the moving-least-squares approximations. The higher-order and smoothness properties of the mesh-free approximation provide a better fit to the real shell geometry. A co-rotational, updated Lagrangian procedure is presented to handle arbitrarily large rotations with moderate strain responses of the shell structures. A local boundary integration method in conjunction with the selective reduced integration method is introduced to enforce the linear exactness and relieve shear locking.

The outline of this paper is as follows. In Section 2, the mesh-free shell surface representation is described. Section 3 presents the updated Lagrangian formulation and the underlying co-rotational procedure for geometrical and material nonlinear shell analysis. In Section 4, numerical examples are given. Both static and dynamic examples are presented.

2. Mesh-free Shell Surface Representation

Surface reconstruction from disorganized nodes is very challenging in three dimensions. The problem is ill posed, i.e., there is no unique solution. Lancaster et al. [13] first proposed a fast surface reconstruction using moving least squares method. Their approach was then applied to the computational mechanics under the name ‘mesh-free method’. Implicitly, the mesh-free method uses a combination of smooth basis functions (primitives) to find a scalar function such that all data nodes are close to an iso-contour of that scalar function in a global sense. In reality, the shell surface construction using the 3D mesh-free method is inadequate. This is because the topology of the real surface can be very complicated in three dimensions. Without the information on the ordering or connectivity of nodes, the reconstructed surface will not be able to represent shell intersections, exterior boundaries and shape corners.

In our development of mesh-free shells, we assume that a shell surface is described by a finite element mesh. This can be easily accomplished by converting a part of shell finite elements into mesh-free zone. With the connectivity of nodes provided by the finite element mesh, a shell surface can be reconstructed with mesh-free interpolation from the nodal positions

$$\bar{\mathbf{x}} = \tilde{\Psi}_I(\mathbf{X})\mathbf{x}_I \quad (1)$$

where \mathbf{x}_I is the position vector of the finite element node on the shell surface and $\tilde{\Psi}_I(\mathbf{X})$ is the mesh-free shape function. In the above surface representation, a 3D arbitrary shell surface needs to be projected to a 2D plane. We propose two approaches for the projection of mesh-free shell surface:

(1) Global parametric representation: The whole shell surface is projected to a parametric plane and the global parametric coordinates are obtained with a parameterization algorithm from the patch of finite elements.

(2) Local projection representation: A local area of the shell is projected to a plane based on the existing element where the evaluated point is located.

Global Parametric Approach

In the global approach, a mesh-free zone with a patch of finite elements is mapped onto a parametric plane with an angle-based triangular flattening algorithm [14], (see Figure 1). The idea of this algorithm is to compute a projection that minimizes the distortion of the FE mesh angles. The mesh-free shape functions are defined in this parametric domain and given by

$$\tilde{\Psi}_I(\mathbf{X}) = \tilde{\Psi}_I(\xi, \eta) \quad (2)$$

where (ξ, η) is the parametric coordinates corresponding to a point \mathbf{X} .

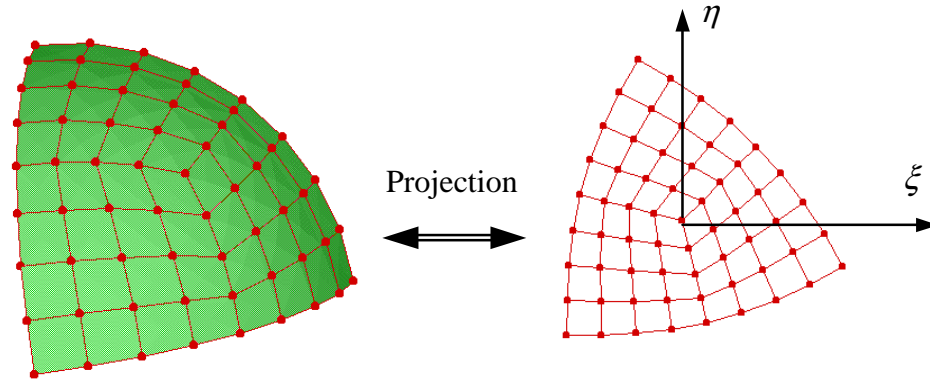


Figure 1: Mesh-free shell global approach

Local Projection Approach

Different from the parameterization algorithm that constructs the surface globally, we reconstruct the surface locally by projecting the surrounding nodes onto the element. In the local projection method, nodes in elements neighboring the element where the evaluated point is located (for example, the element i in Figure 2) are projected onto the plane where the element defines (the “M-plane” in Figure 2). In this figure, $(\hat{x}, \hat{y}, \hat{z})_i$ is a local system defined for each projected plane and $(\bar{x}, \bar{y}, \bar{z})_I$ is a nodal coordinate system defined for each node where \bar{z} is the initial averaged normal direction.

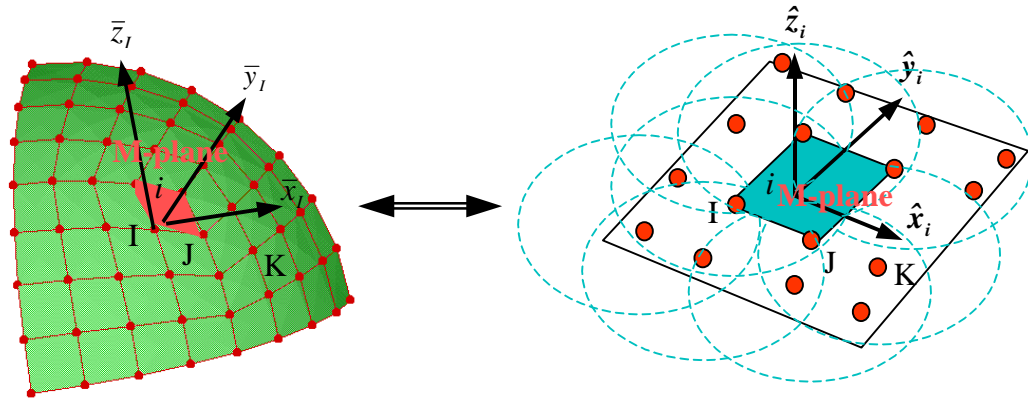


Figure 2: Mesh-free shell local projection

The mesh-free shape functions are then defined with those locally projected coordinates of the nodes

$$\Psi_I(\mathbf{X}) = \Psi_I(\hat{x}, \hat{y}) \quad (3)$$

However, the shape functions obtained directly above are non-conforming, i.e.

$$\Psi_I(\mathbf{X}_J)|_{\text{M-plane}} \neq \Psi_I(\mathbf{X}_J)|_{\text{N-plane}} \quad (4)$$

When the shell structure degenerates to a plate, the constant stress condition cannot be recovered. To remedy this problem, an area-weighted smoothing across different projected planes is used to obtain the conforming shape functions that are given by

$$\tilde{\Psi}_I(\mathbf{X}) = \tilde{\Psi}_I(\hat{x}, \hat{y}) = \frac{\sum_{i=1}^{NIE} \Psi_I(\hat{x}_i, \hat{y}_i) A_i}{\sum_{i=1}^{NIE} A_i} \quad (5)$$

where NIE is the number of surrounding projected planes that can be evaluated at point \mathbf{X} , A_i is the area of the element i , and (\hat{x}_i, \hat{y}_i) is the local coordinates of point \mathbf{X} in the projected plane i .

With this smoothing technique, we can prove that the modified shape functions satisfy at least the *partition of unity* property in the general shell problems. This property is important for the shell formulation to preserve the rigid-body translation.

When the shell degenerates to a plate, we can also prove that the shape functions obtained from this smoothing technique will meet the n -th order completeness condition as

$$\sum_{I=1}^{NP} \tilde{\Psi}_I(\mathbf{X}) X_{1I}^i X_{2I}^j X_{3I}^k = X_1^i X_2^j X_3^k, \quad i + j + k = n \quad (6)$$

This is a necessary condition for the plate to pass the constant bending patch test.

3. Updated Lagrangian Formulation and Co-rotational Procedure

The mesh-free shell formulation is based on the Mindlin-Reissner plate theory, thus the geometry and kinematical fields of the shell can be described with the reference surface and fiber direction. The modified Mindlin-Reissner assumption requires that the motion and displacement of the shell are linear in the fiber direction. Assume that the reference surface is the mid-surface of the shell, the global coordinates and displacements at an arbitrary point within the shell body are given by

$$\mathbf{x} = \bar{\mathbf{x}} + \zeta \frac{h}{2} \mathbf{V}_3 \quad (7)$$

$$\mathbf{u} = \bar{\mathbf{u}} + \zeta \frac{h}{2} \mathbf{U} \quad (8)$$

where $\bar{\mathbf{x}}$ and $\bar{\mathbf{u}}$ are the position vector and displacement of the reference surface, respectively. \mathbf{V}_3 is the fiber director and \mathbf{U} is the displacement resulting from the fiber rotation (see Figures 3 and 4). h is the length of the fiber.

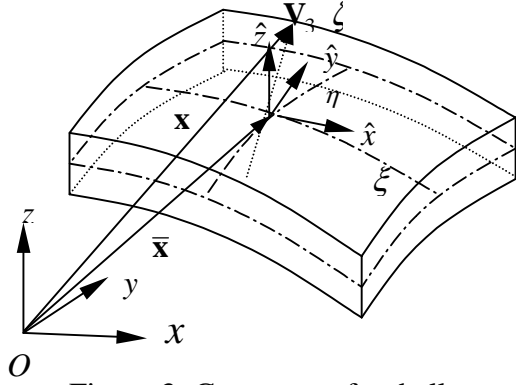


Figure 3: Geometry of a shell.

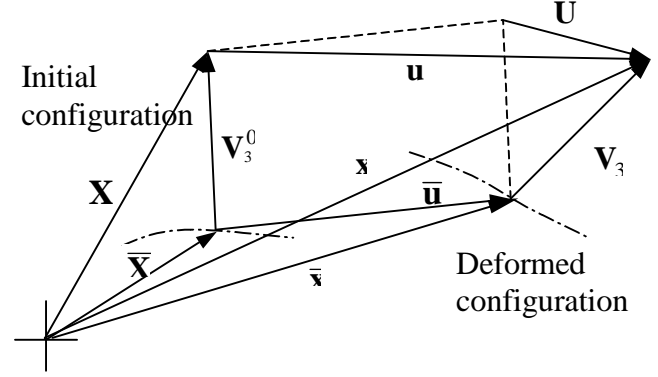


Figure 4: Deformation of a shell.

With the mesh-free approximation, the motion and displacements are given by

$$\mathbf{x}(\xi, \eta, \zeta) = \bar{\mathbf{x}}(\xi, \eta) + \mathbf{V}(\xi, \eta, \zeta) \approx \sum_{I=1}^{NP} \tilde{\Psi}_I(\xi, \eta) \mathbf{x}_I + \sum_{I=1}^{NP} \tilde{\Psi}_I(\xi, \eta) \frac{\zeta h_I}{2} \mathbf{V}_{3I} \quad (9)$$

$$\mathbf{u}(\xi, \eta, \zeta) = \bar{\mathbf{u}}(\xi, \eta) + \mathbf{U}(\xi, \eta, \zeta) \approx \sum_{I=1}^{NP} \tilde{\Psi}_I(\xi, \eta) \mathbf{u}_I + \sum_{I=1}^{NP} \tilde{\Psi}_I(\xi, \eta) \frac{\zeta h_I}{2} [-\mathbf{V}_{2I} \quad \mathbf{V}_{1I}] \begin{Bmatrix} \alpha_I \\ \beta_I \end{Bmatrix} \quad (10)$$

where \mathbf{x}_I and \mathbf{u}_I are the global coordinates and displacements at mesh-free node I , respectively. \mathbf{V}_{3I} is the unit vector of the fiber director and \mathbf{V}_{1I} , \mathbf{V}_{2I} are the base vectors of the nodal coordinate system at node I . α_I and β_I are the rotations of the director vector \mathbf{V}_{3I} about the \mathbf{V}_{1I} and \mathbf{V}_{2I} axes. h_I is the thickness. The variables with a superscripted bar refer to the shell mid-surface. $\tilde{\Psi}_I$ is the 2D mesh-free shape functions constructed based on one of the two mesh-free surface representations described in the previous section, with (ξ, η) either the parametric coordinates or local coordinates of the evaluated point.

The local co-rotational coordinate system $(\hat{x}, \hat{y}, \hat{z})$ is defined at each integration point on the shell reference surface, with \hat{x} and \hat{y} tangent to the reference surface and \hat{z} in the thickness direction (see Figure 5). The base vectors are given as

$$\hat{\mathbf{e}}_1 = \frac{\mathbf{x}_{,\xi}}{\|\mathbf{x}_{,\xi}\|}, \quad \hat{\mathbf{e}}_3 = \frac{\mathbf{x}_{,\xi} \times \mathbf{x}_{,\eta}}{\|\mathbf{x}_{,\xi} \times \mathbf{x}_{,\eta}\|}, \quad \hat{\mathbf{e}}_2 = \hat{\mathbf{e}}_3 \times \hat{\mathbf{e}}_1 \quad (11)$$

In order to describe the fiber rotations of a mesh-free node in a shell, we introduce a nodal coordinate system whose three base vectors are \mathbf{V}_1 , \mathbf{V}_2 and \mathbf{V}_3 , see Figure 5, where \mathbf{V}_3 is the fiber director at the node and \mathbf{V}_1 , \mathbf{V}_2 are defined as follows

$$\mathbf{V}_1 = \frac{\hat{\mathbf{x}} \times \mathbf{V}_3}{\|\hat{\mathbf{x}} \times \mathbf{V}_3\|}, \quad \mathbf{V}_2 = \mathbf{V}_3 \times \mathbf{V}_1 \quad (12)$$

The rotation of the fiber director is then obtained from the global rotations:

$$\begin{Bmatrix} \alpha \\ \beta \end{Bmatrix} = \begin{bmatrix} \mathbf{V}_1^T \\ \mathbf{V}_2^T \end{bmatrix} \Delta \boldsymbol{\theta}, \quad \Delta \boldsymbol{\theta} = [\Delta \theta_1 \quad \Delta \theta_2 \quad \Delta \theta_3]^T \quad (13)$$

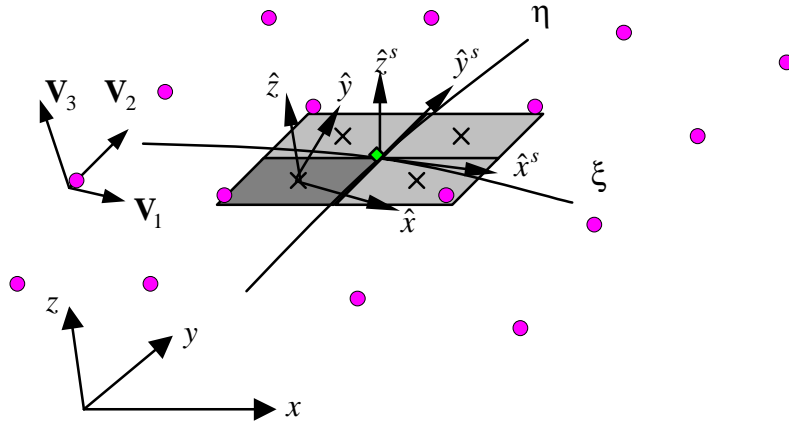


Figure 5: Local co-rotational and nodal coordinate systems.

In the local co-rotational coordinate system, the motion and displacements are approximated by the mesh-free shape functions

$$\hat{x}_i = \sum_{l=1}^{NP} \tilde{\Psi}_l \hat{x}_{il} + \zeta \sum_{l=1}^{NP} \tilde{\Psi}_l \frac{h_l}{2} \hat{V}_{3il} \quad (14)$$

$$\hat{u}_i = \sum_{l=1}^{NP} \tilde{\Psi}_l \hat{u}_{il} + \zeta \sum_{l=1}^{NP} \tilde{\Psi}_l \frac{h_l}{2} \begin{bmatrix} -\hat{V}_{2il} & \hat{V}_{1il} \end{bmatrix} \begin{Bmatrix} \alpha_l \\ \beta_l \end{Bmatrix} \quad (15)$$

The Lagrangian smoothed strains [8] are given by

$$\tilde{\boldsymbol{\epsilon}}^m = \sum_I \tilde{\mathbf{B}}_I^m \hat{\mathbf{d}}_I, \quad \tilde{\boldsymbol{\epsilon}}^b = \zeta \sum_I \tilde{\mathbf{B}}_I^b \hat{\mathbf{d}}_I, \quad \tilde{\boldsymbol{\epsilon}}^s = \sum_I \tilde{\mathbf{B}}_I^s \hat{\mathbf{d}}_I \quad (16)$$

where the smoothed strain operators are calculated by averaging the consistent strain operators over an area around the evaluated point

$$\tilde{\mathbf{B}}_I^m(\mathbf{x}_I) = \frac{1}{A_I} \int_{\Omega_I} \hat{\mathbf{B}}_I^m dA, \quad \tilde{\mathbf{B}}_I^b(\mathbf{x}_I) = \frac{1}{A_I} \int_{\Omega_I} \hat{\mathbf{B}}_I^b dA, \quad \tilde{\mathbf{B}}_I^s(\mathbf{x}_L) = \frac{1}{A_L} \int_{\Omega_L} \hat{\mathbf{B}}_I^s dA \quad (17)$$

with

$$\hat{\mathbf{B}}_I^m = \begin{bmatrix} \tilde{\Psi}_{I,x} & 0 & 0 & -J_{13}^{-1}\tilde{\Psi}_I \frac{h_I}{2} \hat{V}_{2,xI} & J_{13}^{-1}\tilde{\Psi}_I \frac{h_I}{2} \hat{V}_{1,xI} \\ 0 & \tilde{\Psi}_{I,y} & 0 & -J_{23}^{-1}\tilde{\Psi}_I \frac{h_I}{2} \hat{V}_{2,yI} & J_{23}^{-1}\tilde{\Psi}_I \frac{h_I}{2} \hat{V}_{1,yI} \\ \tilde{\Psi}_{I,y} & \tilde{\Psi}_{I,x} & 0 & -J_{23}^{-1}\tilde{\Psi}_I \frac{h_I}{2} \hat{V}_{2,xI} - J_{13}^{-1}\tilde{\Psi}_I \frac{h_I}{2} \hat{V}_{2,yI} & J_{23}^{-1}\tilde{\Psi}_I \frac{h_I}{2} \hat{V}_{1,xI} + J_{13}^{-1}\tilde{\Psi}_I \frac{h_I}{2} \hat{V}_{1,yI} \end{bmatrix} \quad (18a)$$

$$\hat{\mathbf{B}}_I^b = \begin{bmatrix} 0 & 0 & 0 & -\tilde{\Psi}_{I,x} \frac{h_I}{2} \hat{V}_{2,xI} & \tilde{\Psi}_{I,x} \frac{h_I}{2} \hat{V}_{1,xI} \\ 0 & 0 & 0 & -\tilde{\Psi}_{I,y} \frac{h_I}{2} \hat{V}_{2,yI} & \tilde{\Psi}_{I,y} \frac{h_I}{2} \hat{V}_{1,yI} \\ 0 & 0 & 0 & -\tilde{\Psi}_{I,y} \frac{h_I}{2} \hat{V}_{2,xI} - \tilde{\Psi}_{I,x} \frac{h_I}{2} \hat{V}_{2,yI} & \tilde{\Psi}_{I,y} \frac{h_I}{2} \hat{V}_{1,xI} + \tilde{\Psi}_{I,x} \frac{h_I}{2} \hat{V}_{1,yI} \end{bmatrix} \quad (18b)$$

$$\hat{\mathbf{B}}_I^s = \begin{bmatrix} 0 & 0 & \tilde{\Psi}_{I,y} & -J_{33}^{-1}\tilde{\Psi}_I \frac{h_I}{2} \hat{V}_{2,yI} - J_{23}^{-1}\tilde{\Psi}_I \frac{h_I}{2} \hat{V}_{2,zI} & J_{33}^{-1}\tilde{\Psi}_I \frac{h_I}{2} \hat{V}_{1,yI} + J_{23}^{-1}\tilde{\Psi}_I \frac{h_I}{2} \hat{V}_{1,zI} \\ 0 & 0 & \tilde{\Psi}_{I,x} & -J_{33}^{-1}\tilde{\Psi}_I \frac{h_I}{2} \hat{V}_{2,xI} - J_{13}^{-1}\tilde{\Psi}_I \frac{h_I}{2} \hat{V}_{2,zI} & J_{33}^{-1}\tilde{\Psi}_I \frac{h_I}{2} \hat{V}_{1,xI} + J_{13}^{-1}\tilde{\Psi}_I \frac{h_I}{2} \hat{V}_{1,zI} \end{bmatrix} \quad (18c)$$

and \mathbf{J}^{-1} is the inverse of the Jacobian matrix at the integration point. The local degrees-of-freedom are

$$\hat{\mathbf{d}}_I = [\hat{u}_{xI} \quad \hat{u}_{yI} \quad \hat{u}_{zI} \quad \alpha_I \quad \beta_I]^T \quad (19)$$

The stiffness matrices and load vectors in the local co-rotational coordinate system are defined as follows. The material stiffness matrix is

$$\hat{\mathbf{K}}_{IJ}^M = \hat{\mathbf{K}}_{IJ}^m + \hat{\mathbf{K}}_{IJ}^b + \hat{\mathbf{K}}_{IJ}^s \quad (20)$$

with

$$\hat{\mathbf{K}}_{IJ}^m = \int_{\Omega} \tilde{\mathbf{B}}_I^{mT} \mathbf{C}^m \tilde{\mathbf{B}}_J^m d\Omega, \quad \hat{\mathbf{K}}_{IJ}^b = \int_{\Omega} \tilde{\mathbf{B}}_I^{bT} \zeta^2 \mathbf{C}^b \tilde{\mathbf{B}}_J^b d\Omega, \quad \hat{\mathbf{K}}_{IJ}^s = \int_{\Omega} \tilde{\mathbf{B}}_I^{sT} \mathbf{C}^s \tilde{\mathbf{B}}_J^s d\Omega \quad (21)$$

The geometric stiffness matrix is

$$\hat{\mathbf{K}}_{IJ}^G = \int_{\Omega} \tilde{\mathbf{B}}_{kl}^T \hat{\sigma}_{kl} \tilde{\mathbf{B}}_{IJ} d\Omega \quad (22)$$

with

$$\mathbf{B}_{kl} = \begin{bmatrix} \tilde{\Psi}_{I,k} & 0 & 0 & -(\zeta\tilde{\Psi}_I)_{,k} \frac{h_I}{2} \hat{V}_{2xl} & (\zeta\tilde{\Psi}_I)_{,k} \frac{h_I}{2} \hat{V}_{1xl} \\ 0 & \tilde{\Psi}_{I,k} & 0 & -(\zeta\tilde{\Psi}_I)_{,k} \frac{h_I}{2} \hat{V}_{2yl} & (\zeta\tilde{\Psi}_I)_{,k} \frac{h_I}{2} \hat{V}_{1yl} \\ 0 & 0 & \tilde{\Psi}_{I,k} & -(\zeta\tilde{\Psi}_I)_{,k} \frac{h_I}{2} \hat{V}_{2zl} & (\zeta\tilde{\Psi}_I)_{,k} \frac{h_I}{2} \hat{V}_{1zl} \end{bmatrix} \quad (23)$$

Decomposing the above into constant and linear terms in the function of ζ

$$\mathbf{B}_{kl} = \mathbf{B}_{kl}^0 + \zeta \mathbf{B}_{kl}^1 \quad (24)$$

where

$$\mathbf{B}_{kl}^0 = \begin{bmatrix} \tilde{\Psi}_{I,k} & 0 & 0 & -J_{k3}^{-1} \tilde{\Psi}_I \frac{h_I}{2} \hat{V}_{2xl} & J_{k3}^{-1} \tilde{\Psi}_I \frac{h_I}{2} \hat{V}_{1xl} \\ 0 & \tilde{\Psi}_{I,k} & 0 & -J_{k3}^{-1} \tilde{\Psi}_I \frac{h_I}{2} \hat{V}_{2yl} & J_{k3}^{-1} \tilde{\Psi}_I \frac{h_I}{2} \hat{V}_{1yl} \\ 0 & 0 & \tilde{\Psi}_{I,k} & -J_{k3}^{-1} \tilde{\Psi}_I \frac{h_I}{2} \hat{V}_{2zl} & J_{k3}^{-1} \tilde{\Psi}_I \frac{h_I}{2} \hat{V}_{1zl} \end{bmatrix} \quad (25a)$$

$$\mathbf{B}_{kl}^1 = \begin{bmatrix} 0 & 0 & 0 & -\tilde{\Psi}_{I,k} \frac{h_I}{2} \hat{V}_{2xl} & \tilde{\Psi}_{I,k} \frac{h_I}{2} \hat{V}_{1xl} \\ 0 & 0 & 0 & -\tilde{\Psi}_{I,k} \frac{h_I}{2} \hat{V}_{2yl} & \tilde{\Psi}_{I,k} \frac{h_I}{2} \hat{V}_{1yl} \\ 0 & 0 & 0 & -\tilde{\Psi}_{I,k} \frac{h_I}{2} \hat{V}_{2zl} & \tilde{\Psi}_{I,k} \frac{h_I}{2} \hat{V}_{1zl} \end{bmatrix} \quad (25b)$$

the geometric stiffness matrix can be written as

$$\hat{\mathbf{K}}_{IJ}^G = \int_{\Omega} \mathbf{B}_{kl}^{0T} \hat{\sigma}_{kl} \mathbf{B}_{IJ}^0 d\Omega + \int_{\Omega} \mathbf{B}_{kl}^{0T} \zeta \hat{\sigma}_{kl} \mathbf{B}_{IJ}^1 d\Omega + \int_{\Omega} \mathbf{B}_{kl}^{1T} \zeta \hat{\sigma}_{kl} \mathbf{B}_{IJ}^0 d\Omega + \int_{\Omega} \mathbf{B}_{kl}^{1T} \zeta^2 \hat{\sigma}_{kl} \mathbf{B}_{IJ}^1 d\Omega \quad (25)$$

The internal nodal force vector is

$$\hat{\mathbf{F}}_I^{\text{int}} = \int_{\Omega} \tilde{\mathbf{B}}_I^{mT} \hat{\sigma} d\Omega + \int_{\Omega} \zeta \tilde{\mathbf{B}}_I^{bT} \hat{\sigma} d\Omega + \int_{\Omega} \tilde{\mathbf{B}}_I^{sT} \hat{\sigma} d\Omega \quad (26)$$

The above integrals are calculated with the local boundary integration method [15]. Each background finite element is divided into four integration zones, shown as Ω_I in Figure 6. In order to avoid shear locking in the analysis of thin shells, the shear stiffness (third term in Eq. (20)), should be under-integrated by using one integration zone in each background element (Ω_L in Figure 6). Accordingly, the co-rotational coordinate systems are defined separately at the center of each integration zone, as shown in Figure 5.

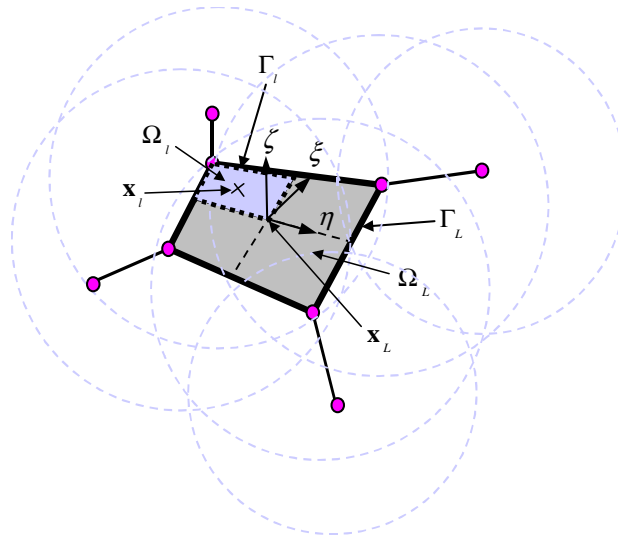


Figure 6: Integration scheme for mesh-free shells.

The use of the updated Lagrangian formulation implies that the reference coordinate system is defined by the co-rotational system in the configuration at time t . Therefore, the local stiffness matrices as well as force and displacement vectors referred to this coordinate system must be transformed to the global coordinate system prior to assemblage.

4. Numerical Examples

Shallow Shell Cap Under Inflation

A double curved shallow shell cap is inflated by pressure loading. The geometric dimension of the shell cap is 32mm long, 24mm wide and 24mm deep. Its thickness is 2mm. The material is elastic, with Young's modulus of 210.0GPa and Poisson's ratio of 0.3. The deformation of the shell cap under inflation is dominated by membrane strain. This problem is used to test the membrane property of the developed implicit mesh-free shells.

The shell cap is discretized by 8×6 elements, as shown in Figure 7. For this rather coarse mesh, the mesh-free local projection method can run up to 8.00ms and the mesh-free global approach can get a converged solution up to 7.62ms with a normalized support size of 1.10. The assumed stress/strain shell element (shell type 16) diverges at 7.79ms. The deformations given by the mesh-free shells and the finite element shell agree very well (see Figure 8).

SHALLOW CAP INFLATION
Time = 0

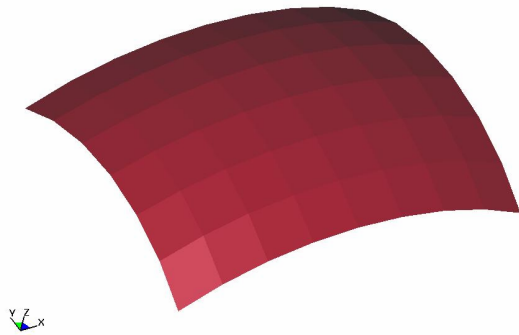


Figure 7: Numerical model for shallow shell cap.

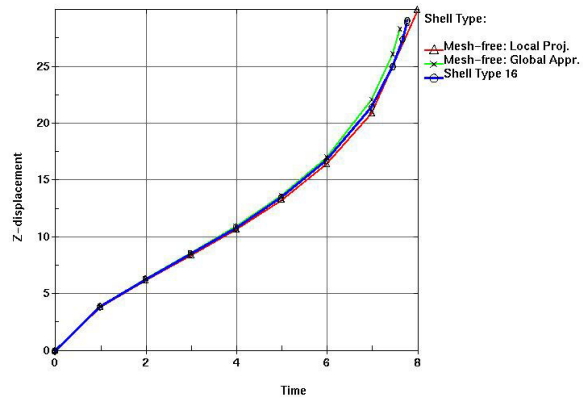


Figure 8: Displacement of center point on the shell cap.

Springback Simulation

A springback simulation specified as Numisheet 93 is performed. A strip of mild steel sheet is subjected to forming process then released from the constraint of the die, punch and holder.

Due to symmetry, only half of the problem domain is modeled in the simulation (see the left picture in Figure 9). The workpiece with dimensions of 175.0mm by 17.5mm and thickness of 0.5mm is discretized to one mesh-free zone with 715 nodes, which will go through large changes of shape and deformation, and two finite element zones with total 648 elements, as shown in the right picture in Figure 9. The material for the workpiece is modeled by transversely anisotropic elasto-plastic material (material type 37).

The forming process is simulated by an explicit analysis with a termination time of 70ms. The springback process is simulated by an implicit analysis to a termination time of 350ms. With a normalized support size of 1.10, the two mesh-free shells can complete the springback simulation with 5 time steps. Figure 10 demonstrates the deformations and contours of the effective stress at four times: 70ms, 140ms, 230ms, and 350ms. The final shape of the workpiece after the springback is shown in Figure 11. The springback angle is 16.40°, which is close to the experimental value of 17.10°. The time history of the springback angle is shown in Figure 12.

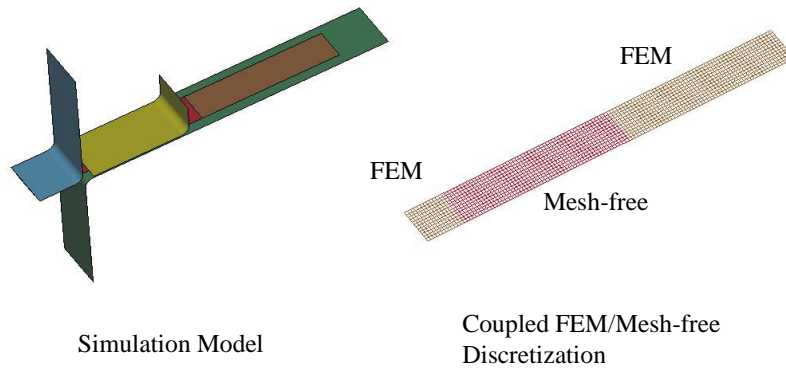


Figure 9: Problem description of springback simulation.

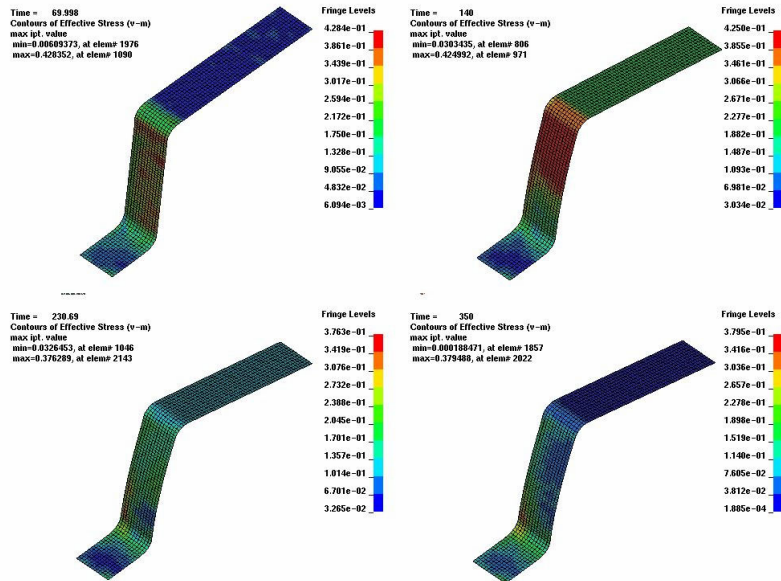


Figure 10: Contours of effective stress at different stages of springback.

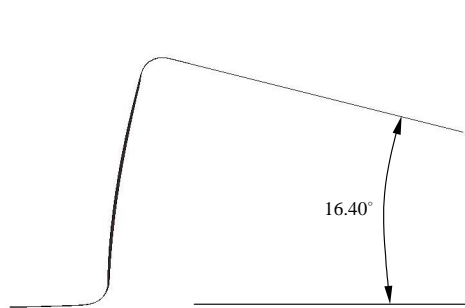


Figure 11: Final shape of workpiece after springback.

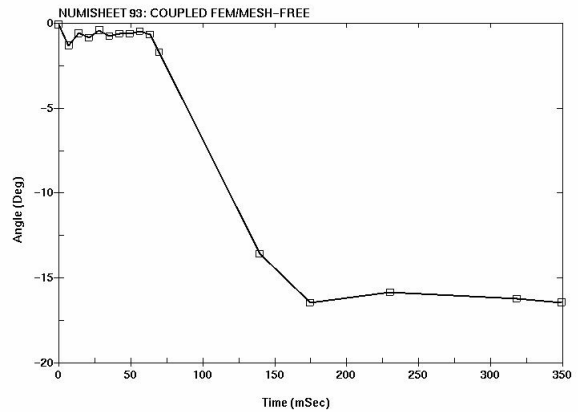


Figure 12: Change of angle of the workpiece.

Boxbeam Simulation

This is a classical impact problem to measure the crushing forces of the hollow structures. A steel boxbeam with an initial cross section 38.1 cm by 50.8 cm and an initial height 203 cm is subjected to an impact force as shown in Figure 13. The initial thickness of the cross section is 0.914mm. The impact force is prescribed by a rigid block with a constant velocity 1.28 m/s. Due to symmetry, only one quarter of the model is analyzed. The material properties of the boxbeam are given in Table 1.

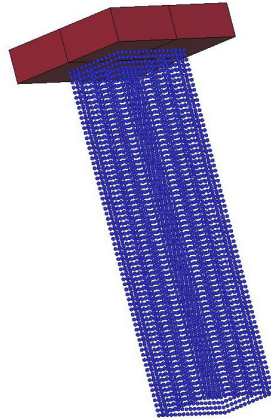


Figure 13: Boxbeam model

Table 1.

Mass density	Young's modulus	Poission's ratio	Yield stress	Tangent modulus	Hardening parameter
7.83e-9	2.1e+5	0.3	206.0	206.0	1.0

Explicit time integration method with row-sum mass matrix is employed. A comparison between the numerical result using two mesh-free methods and two finite element methods (element type 8 and element type16) are given.

The comparison of crushing force is displayed in Figure 14. All four numerical methods give similar results. Four consecutive deformed geometries are plotted in Figure 15. The dynamic plastic bulking pattern obtained from the mesh-free method agrees well with the finite elements result.

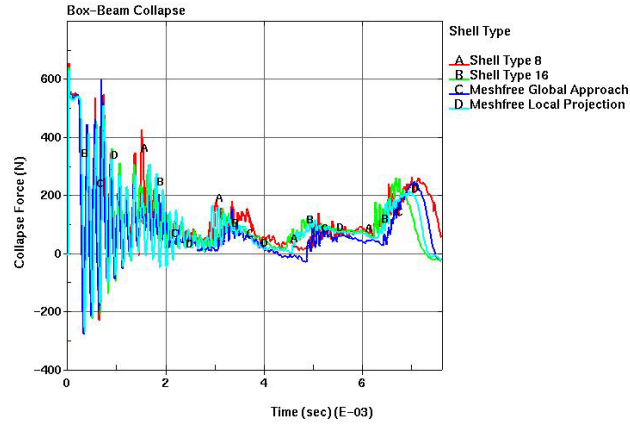


Figure 14: Comparison of crushing force

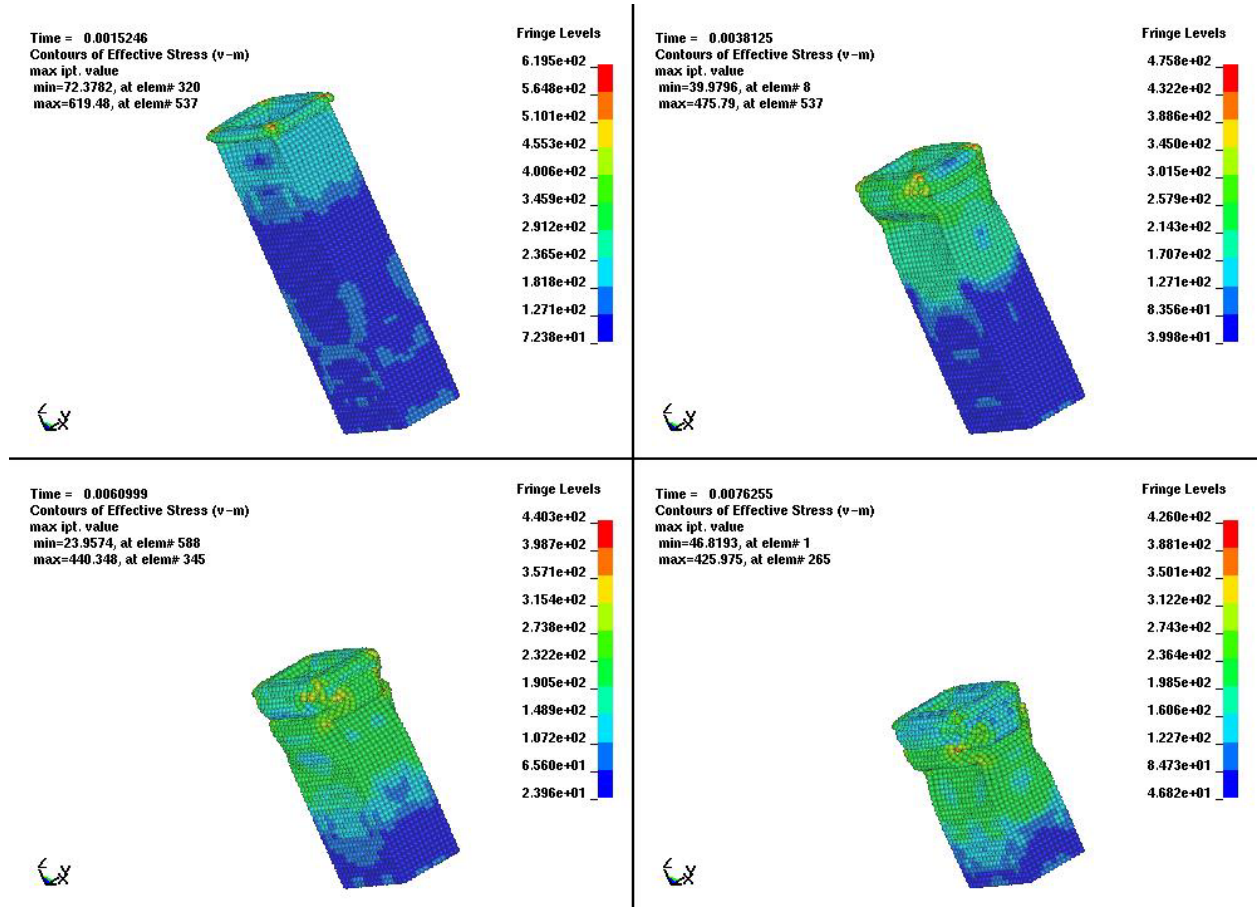


Figure 15: Contours of effective stress at different deformed stage.

Acknowledgements

The support of this research by GM R&D Center to LSTC is greatly acknowledged.

References

1. Belytschko, T., Lu, Y. Y., and Gu, L., "Element-free Galerkin Methods", p229-256, 37, International Journal for Numerical Methods in Engineering (1994).
2. Liu, W. K., Jun, S., Li, S., Adee, J., and Belytschko, B., "Reproducing Kernel Particle Methods for Structural Dynamics", p1655-1679, 38, International Journal for Numerical Methods in Engineering (1995).
3. Chen, J. S., Pan, C., Wu, C. T., and Liu, W. K., "Reproducing Kernel Particle Methods for Large Deformation Analysis of Nonlinear Structures", p195-227, 139, Computer Methods in Applied Mechanics and Engineering (1996).
4. Duarte, C. A., and Oden, J. T., "H-p Clouds: An H-p Meshless Method", p673-705, 12, Numerical Methods in Partial Differential Equations (1996).
5. Babuska, I. and Melenk, J. M., "The Partition of Unity Method", p727-758, 40 (1996).
6. Gunther, F. and Liu, W. K., "Admissible Approximations for Essential Boundary Conditions in the Reproducing Kernel Particle Method", p205-230, 163, Computer Methods in Applied Mechanics and Engineering (1998).
7. Chen, J.S. and Wang, H. P., "New Boundary Condition Treatments for Meshless Computation of Contact Problems", p441-468, 187, Computer Methods in Applied Mechanics and Engineering (2001).
8. Chen, J. S., Wu, C. T., Yoon, S., and You, Y., "A Stabilized Conforming Nodal Integration for Galerkin Meshfree Methods", p435-466, 50, International Journal for Numerical Methods in Engineering (2001).
9. Wu, C. T. and Guo, Y., "Development of Coupled Finite Element/Mesh-free Method and Mesh-free Shell Formulation", Technical Report, GM R&D Center (2002).
10. Krysl, P. and Belytschko, T., "Analysis of Thin Shells by the Element-free Galerkin Method", p 3057-3080, 33, International Journal of Solids and Structures (1996).
11. Noguchi, H., Kawashima, T. and Miyamura, T., "Element Free Analysis of Shell and Spatial Structures", p1215-1240, 47, International Journal for Numerical Methods in Engineering (2000).
12. Meek, J. L. and Wang, Y., "Nonlinear Static and Dynamic Analysis of Shell Structures with Finite Rotation", p301-315, 162, Computer Methods in Applied Mechanics and Engineering (1998).
13. Lancaster, P. and Salkauskas, K., "Surfaces generated by moving least squares methods", p141-158, 37, Math. Comput (1981).
14. Sheffer, A. and de Sturler, E. "Parameterization of faceted surfaces for meshing using angle-based flattening", p326-337, 17, Engineering with Computers (2001).
15. Wu, C. T., Guo, Y., Wang, H. P. and Botkin, M. K., "A coupled finite element and mesh-free method for solid and shell dynamic explicit analysis", International Journal for Numerical Methods in Engineering, to submit.